# The Electrical Conductivity of Liebermannite: Implications for Water Transport Into the Earth's Lower Mantle

Geeth Manthilake, Federica Schiavi, Chengcheng Zhao, Mainak Mookherjee, Mohamed Ali M.A. Bouhifd, Laurent Jouffret

# The electrical conductivity of liebermannite: Implications for water transport into the Earth's lower mantle

Geeth Manthilake[1*], Federica Schiavi[1], Chengcheng Zhao[1], Mainak Mookherjee[2], Mohamed Ali Bouhifd[1], Laurent Jouffret[3]

[1] Laboratoire Magmas et Volcans, CNRS, IRD, OPGC, Université Clermont Auvergne, 63000 Clermont-Ferrand, France

[2] Earth Materials Laboratory, Department of Earth, Ocean and Atmospheric Sciences, Florida State University, Tallahassee, FL, 32306, USA

[3] Laboratoire des Matériaux et du Génie Physique, UMR 5628, 3 parvis Louis Néel - CS50257 - 38016 Grenoble, France

[*]**Corresponding author:** Geeth Manthilake (geeth.manthilake@uca.fr)

**Key Points:**

- The hopping of $K^+$ ions in liebermannite results in high electrical conductivity of more than 1 S/m.
- Water can be present as both molecular $H_2O$ and hydroxyl ($OH^-$) groups in liebermannite
- High $H_2O$ contents of ocean island basalts can be related to deeply subducted hydrous liebermannite

## Abstract

Liebermannite ($KAlSi_3O_8$) is a principal mineral phase expected to be thermodynamically stable in deeply subducted continental and oceanic crusts. The crystal structure of liebermannite exhibits tunnels that are formed between the assemblies of double chains of edge-sharing (Si, Al) $O_6$ octahedral units, which act as a repository for large incompatible alkali ions. In this study, we investigate the electrical conductivity of liebermannite at 12, 15, and 24 GPa and temperature of 1500 K to track subduction pathways of continental sediments into the Earth's lower mantle. Further, we looked at whether liebermannite could sequester incompatible $H_2O$ at deep mantle conditions. We observe that the superionic conductivity of liebermannite due to the thermally activated hopping of $K^+$ ions results in high electrical conductivity of more than 1 S/m. Infrared spectral features of hydrous liebermannite indicate the presence of both molecular $H_2O$ and hydroxyl ($OH^-$) groups in its crystal structure. The observed high electrical conductivity in the mantle transition zone beneath Northeastern China and the lower mantle beneath the Philippine Sea can be attributed to the subduction pathways of continental sediments deep into the Earth's mantle. While major mineral phases in pyrolitic compositions are almost devoid of $H_2O$ under lower mantle conditions, our study demonstrates that liebermannite could be an important host of $H_2O$ in these conditions. We propose that the relatively high $H_2O$ contents of ocean island basalts derived from deep mantle plumes are primarily related to deeply subducted continental sediments, in which liebermannite is the principal $H_2O$ carrier.

## Plain Language Summary

Liebermannite ($KAlSi_3O_8$, formally K-hollandite) is an important mineral phase in deeply subducted continental and oceanic crusts. Liebermannite exhibits high ionic conductivity and could explain low resistivity in the Earth's mantle transition zone and the upper part of the lower mantle, hinting towards the subduction of hydrated crusts into the lower mantle. The libermannite samples synthesized at these conditions indicate the presence of both molecular $H_2O$ and hydroxyl ($OH^-$) groups in its crystal structure, suggesting that liebermannite could be an important host of $H_2O$ in the Earth's deep mantle. Compared to the basalts from mid-ocean ridges that exhibit trace quantities of water, ocean island basalts show higher water contents. It has been speculated that ocean basalts are derived from crustal components that were deeply subducted. It is also known that the lower mantle is relatively dry. Therefore, it is difficult to reconcile the higher water contents in OIBs that are derived from the deep mantle. Here, we demonstrate that the source crustal components for OIBs were likely to be hydrated. Libermannite is a key mineral in deeply subducted crusts and can efficiently host water.

## 1. Introduction

Trace quantities of $H_2O$ stored in the Earth's mantle significantly influence the physical properties of mantle rocks (Smyth & Jacobsen, 2006). Although $H_2O$ plays an important role by affecting both mineral properties and mantle dynamics of the upper mantle, it is well known that the Earth's lower mantle is relatively dry, as indicated by the low (< 1000 ppm wt.) $H_2O$ solubility in major lower mantle mineral phases (Bolfan-Casanova et al., 2003; Fu et al., 2019; Hirschmann, 2006). Yet some oceanic island basalts (OIB), which are characterized by relatively high $H_2O$ contents up to ~ 2.0 wt. %, are fed by plumes rising from the lower mantle (Deschamps et al., 2011). These plumes are thought to originate from enriched reservoirs composed of recycled crustal materials that subducted into the deep mantle (Willbold & Stracke, 2006). Hydrous phases associated with subducting slabs descending into the lower mantle (van der Hilst et al., 1997) may provide a plausible mechanism for transporting $H_2O$ into the deep mantle. Dense hydrous magnesium silicates (DHMS), such as phase H and phase D, which are known to be stable in the depleted portion of the subducting slab at lower mantle conditions, are likely to transport $H_2O$ into the lower mantle and subsequently hydrate the subducted crustal components (Nishi et al., 2014; Pamato et al., 2014).

While the dominant component of all OIB is likely to be recycled basaltic oceanic crust, both chemical and isotopic signatures of OIB indicate the mixing of different source materials (Hart, 1988). Particularly the Enriched Mantle II (EMII)-type OIB, which have been found in the Society Islands, the Marquesas and Samoa, suggest a 5-10 % of continental and sedimentary components (Hart, 1988). Water contents up to 1.5 wt. % and low $H_2O$/Ce (<150) have been reported in such EMII-type OIB (Cabral et al., 2014). The estimates based on geochemical analyses indicate that $H_2O$ concentrations in EMII sources are about 400 ppm wt. (Dixon et al.,

2002). The low $H_2O$/Ce measured in EM-type magmas indicates up to 92 % $H_2O$ loss from the recycled continental components with progressive dehydration (Dixon et al., 2002). Despite intense dehydration, the deeply subducted slab appears to retain or rehydrate by the dehydration of dense hydrous phases such that a sufficient amount of $H_2O$ is available in the deep OIB sources (Dixon et al., 2002).

Liebermannite, formerly known as Liebermannite, is the high-pressure polymorph of $KAlSi_3O_8$-feldspar and is likely to be stable in deeply subducted (> 300 km) continental crust and mid-oceanic ridge basalt compositions enriched in potassium (Schmidt, 1996). The crystal structure of liebermannite exhibits tunnels that are formed between the assemblies of double chains of edge-sharing (Si, Al)$O_6$ octahedral units. At pressures ≤ 20-23 GPa, liebermannite (*lowP*) crystallizes in a tetragonal (*I*4/*m*) space group symmetry, whereas above these pressures, the tunnels are slightly squeezed, and the high-pressure polymorph of liebermannite (*hiP*) crystallizes in a monoclinic (*I*2/*m*) space group symmetry (Ferroir et al., 2006; Nishiyama et al., 2005). These tunnels accommodate incompatible cations such as Na, K, Sr, Ba, La, and Pb. A naturally occurring liebermannite containing $Ba^{2+}$ and $K^+$ is reported to contain up to 5 wt. % $H_2O$ in its crystal structure (Miura, 1986), indicating that liebermannite could be an important host for $H_2O$. The *hiP* polymorph is observed to be stable down to the Earth's lowermost mantle conditions (Kawai & Tsuchiya, 2013; Sueda et al., 2004). At mantle transition zone conditions, phase equilibria studies indicate that average continental crust is composed of a mixture of liebermannite (~32 vol. %), stishovite (24 vol.%), majoritic garnet (30 vol. %) and minor amounts of calcium aluminosilicate (CAS) phases (Irifune et al., 1994).

The presence of tunnels in the crystal structure of liebermannite facilitates the motion of $K^+$ ions along the channel, attaining superionic conduction at high temperatures (Furusawa et al.,

1988; Khanna et al., 1981; Yoshikado et al., 1982). More recently, the electrical conductivity of liebermannite, relevant for the deeply subducted crust, has been examined using molecular dynamics simulations. The predicted electrical conductivity for liebermannite with a 12.5 % vacancy in the tunnel is ~20 S/m at 10 GPa and 1600 K (He et al., 2016). The magnitude of the predicted electrical conductivity resulting from ionic conduction of $K^+$ ions in the tunnels is significantly greater than that of the electrical conductivity due to extrinsic defects. Hence, owing to its high electrical conductivity, liebermannite potentially represents an ideal tracer mineral for tracking subducted pathways of continental crustal components into the Earth's lower mantle.

The unique crystal structure of liebermannite and the ability to accommodate large alkali ions and possibly $H_2O$ in its tunnels highlight its importance as a possible $H_2O$ repository in the subducted crustal components and a possible source for OIB. However, so far, studies on liebermannite have been restricted to the equation of state, elasticity (Caracas & Boffa Ballaran, 2010; Kawai & Tsuchiya, 2013; Mookherjee & Steinle-Neumann, 2009), and electrical conductivity (He et al., 2016) of the dry variety.

In this study, we first conducted high-pressure and temperature experiments to constrain the electrical conductivity of hydrous liebermannite at the upper mantle, transition zone, and lower mantle conditions, i.e., at pressures of 12, 15, and 24 GPa respectively. Then we examined the water incorporation mechanisms in liebermannite. Finally, we explore whether the high $H_2O$ contents of OIB could have derived from hydrated crustal components of deeply subducted slabs penetrated down to the lower mantle.

## 2. Materials and Methods

The starting powder was prepared using high purity oxide mixtures of $K_2CO_3$, $Al_2O_3$, and $SiO_2$. The mixture was slowly heated to 1000 °C overnight in a platinum crucible for decarbonate $K_2CO_3$. The decarbonated powdered mixture was then heated to 1500 °C and kept 10 minutes to obtain homogeneous glass. The time was optimized to avoid possible K loss at high temperatures.

High pressure-high temperature experiments were conducted using a 1500-ton multi-anvil apparatus. The pre-synthesis of K-feldspar for electrical conductivity measurements were conducted at 2 GPa and 1200 K in a 14/8 assmbly (Fig. 1a). To synthesize hydrous K-feldspar we add $Al(OH)_3$ to the glass mixture to obtain ~ 100 wt. ppm $H_2O$. The powdered mixture was packed into a capsule made of rhenium (Re), and kept ant high-pressure and high-temperaure for durations of 4 hours to obtain the cylindrical samples for electrical conductivity measurements. The water contents of K-feldspar is measured to be 257±29 wt. ppm.

The pressure and temperature conditions for the electrical conductivity measurements were carefully chosen based on the stability liebermannite (Nishiyama et al., 2005) and represent the upper mantle (12 GPa), mantle transition zone (15 GPa), and the upper part of the lower mantle (24 GPa). Electrical conductivity measurements were performed using octahedral pressure medium composed of MgO and $Cr_2O_3$ (5 wt. %) in a 14/8 assembly (octahedron edge length/anvil truncation edge length) at 12 GPa, in a 14/6 assembly at 15 GPa, and a 10/4 assembly at 24 GPa (Fig.1b). MgO ceramic sleeves insulated the electrode wires from the furnace. All ceramic assembly parts, including the pressure media, were baked at 1000 °C for more than 12 hours and tthen stored at 125 °C in high- vacuum furnaces (< 100 mTorr) before assembling. This step reduces the exposure of assembly components to atmospheric moisture and other impurities.The sample temperature was measured using a type-C tungsten-rhenium (W95Re5-W74Re26)

thermocouple junction, placed at one end of the sample. One cable formed the thermocouple and a separate $W_{95}Re_5$ cable placed at the opposite side of the sample connected to the impedance spectroscopy for the electrical conductivity measurements.

The electrical conductivity of liebermannite samples was determined using the impedance spectroscopy method using the Modulab MTS Impedance gain-phase analyzer. The frequency range for the analyses was $10^6$-$10^1$ Hz. After compressing the assembly to the desired pressure, samples were heated to 500 K and while maintaining a temperature of 500 K, the electrical resistance of the sample was measured regularly until the sample resistance reached a stable value. The decrease of electrical resistance observed at this step corresponds to the removal of the absorbed moisture in the sample capsule and the surrounding area, which could be incorporated into the sample at higher temperatures (Manthilake et al., 2015). During the measurements, sample resistance was determined in several heating and cooling cycles until the electrical resistance of heating and cooling paths become reproducible. For the discussion, we have used the data from the last cooling cycle, which minimizes the uncertainty in electrical conductivity. The sample resistance can be obtained by fitting the impedance spectra with an appropriate equivalent circuit. For polycrystalline samples, as we use in this study, the equivalent circuit can be illustrated by a combination of resistor-capacitor/constant phase element (R-C/CPE) components, connected in parallel, series, or a series-parallel combination. Once the electrical resistivity of the samples was determined from the fit of the impedance spectra, the electrical conductivity was determined using the radius and the axial length of the cylindrical sample measured after each experiment. The inherent assumption is that the sample geometry remained constant during the experiment.

The chemical compositions the experimental run products were investigated using a Cameca SxFiveTactis electron probe microanalyzer (EPMA) in wavelength dispersive (WDS)

192 mode operating at an accelerating voltage of 15 kV and 4 nA beam current. The low accelerating
193 voltage was used to avoid the K loss in liebermannite.

194 Powder X-ray diffraction (PXRD) analyses of experimental run products were carried out
195 to identify the crystal structures of liebermannite and the phases present in quenched samples at
196 15 and 24 GPa. The PXRD was obtained for ~1 $mm^3$ of crushed samples that were placed on zero-
197 background Si sample holders. The PXRD was recorded using a Philipps X-Pert Pro diffractometer
198 with $CuK_\alpha$ radiation source ($\lambda = 0.15405$ nm). The PXRD patterns were recorded over the 10–90°
199 (2θ) range in steps of 0.0167° with a counting time of 700 s per step. Lattice parameters were
200 obtained from LeBail fits using the FULLPROF program (Rodriguez-Carvajal, 1993). The
201 background can be obtained by linear interpolation between twenty-six points, and the peak
202 profiles were modeled using a pseudo-Voigt function.

203 Raman spectroscopy was used to identify liebermannite and the minor mineral phases
204 present in the experimental run products. Raman spectra were collected in a back-scattered
205 geometry using an InVia confocal Raman micro-spectrometer, equipped with a 532 nm diode laser,
206 a Peltier-cooled CCD detector, a Rayleigh rejection edge filter (Schiavi et al., 2018). The laser
207 power of 1-8 mW; the slit aperture of 65 $\mu$m, and a grating of 2400 l/mm were used for the present
208 analyses. These conditions result in lateral and axial spatial resolutions of ~1 and 3 $\mu$m and a
209 spectral resolution of 1 $cm^{-1}$. Acquisition times were 30-60 s and 60-240 s for the low-wavenumber
210 and high-wavenumber region, respectively.

211 The quantification of $H_2O$ in liebermannite was performed using the Fourier Transform
212 Infrared (FTIR) spectroscopy. Unpolarized FTIR spectra of liebermannite were acquired using a
213 Vertex70 Bruker spectrometer equipped with a Globar light source, a KBr beamsplitter, and an
214 MCT (Mercury-Cadmium-Tellurium alloy) detector. The beam size for the analyses was ~ 30 µm.

The spectra were obtained through a $CaF_2$ window with a resolution of 4 $cm^{-1}$. About 2000 scans were accumulated for a single spectrum. Thin slabs were cut perpendicular to the compression axis of the experimental run products using a high-precision diamond wire saw and polished using diamond mats without acetone or bond materials, such as crystal-bond or orthodontic adhesive paste to avoid IR signal contaminations. Being the samples polycrystalline, it was not possible to perform polarized measurements on single crystals; therefore, we estimated the $H_2O$ content of each sample based on several spectra that were taken over many randomly oriented crystals. The spectra were integrated between 2600 and 3800 $cm^{-1}$, an average of several spectra was calculated for each sample and multiplied by a factor 3. The OH content was quantified using the Beer-Lambert law:

$$C_{H2O} = 18.02 \times A \times 10^6 / \varepsilon \times t \times \rho$$

where $C_{H2O}$ is the concentration of hydrous species expressed in ppm $H_2O$ by weight, 18.02 is the molecular weight of $H_2O$; A is the total integrated area of bands in the region of interest, $t$ is the thickness of the sample in cm, $\varepsilon$ is the molar absorption coefficient, and $\rho$ is the density of the sample in g/L. For the estimation of $H_2O$ content in liebermannite, we used the theoretically predicted integral molar absorption coefficient of 250000 L/(mol.$cm^2$) (Koch-Müller & Rhede, 2010).

## 3. Results

The electrical conductivity of liebermannite samples at 12, 15, and 24 GPa are summarized in **Fig. 2**. The discontinuous increase in electrical conductivity at a temperature above 660 K during the first heating cycle of the 12 GPa experiment coincides with the transformation of K-Feldspar to liebermannite with increasing temperature (**Fig. 2a**). This transformation accounts for more than

one order of magnitude increase of conductivity for liebermannite. After the complete transformation, the electrical conductivity of libermannite increases with increasing temperature from 700 K to 1500 K and reached to about 1 S/m at 12 GPa and 1500 K. The increase of pressure appears to have an inverse effect on the electrical conduction in liebermannite (**Fig. 2b**). The impedance spectra of the sample undergoing K-feldspar to libermannite transition with increasing temperature are shown (**Fig. 3**).

The activation enthalpy (ΔH) of each conduction mechanism can be calculated by fitting the data to equation, $\sigma = \sigma_0 exp^{(-\Delta H|RT)}$, where σ is the electrical conductivity (S/m), T is the absolute temperature (K), $\sigma_0$ is the pre-exponential factor (S/m), and R is the gas constant (J/K mol). Here, we analyzed the activation enthalpy, first by manually fitting different temperature segments to the fitting equation and, second, by fitting the equation to the entire temperature range (Fei et al., 2020). The estimated activation enthalpies for different conduction mechanisms obtaine using two fitting methods are listed in **Table 1**.

The EPMA, SEM, and Raman grid-analyses indicate that liebermannite is the principal phase present in samples synthesized at 12, 15, and 24 GPa (**Fig. 4**). However, minor amounts of wadeite, kyanite, and stishovite presence in our samples, an observation consistent with a previous study (Urakawa et al., 1994) (**Table. 2**) (**Fig.5)**. The grid analyses with a step size of 5 μm also confirmed the absence of melt in our samples. The minor phases mostly occur as isolated grains within the libermannite matrix **(Fig 5a)** and the volume fraction of minor phases appeared to decrease with increasing pressure. Chemical analyses of minor phases at the 24 GPa sample were hampered by either absence of minor phases (e.g kyanite) at high-pressure samples or if present, their extremely small grain sizes (< 5μm).

The FTIR analyses of libermannite samples after the electrical conductivity measurements indicate water contents of 1044±87 wt. ppm at 12 GPa, 885±78 wt. ppm at 15 GPa and 1104±18 wt. ppm at 24 GPa (**Fig 6**). The high water contents compared to the K-feldspar starting material suggest that the absorbed moisture in the assembly parts may have been incorporated into the sample during the K-feldspar-libermannite transformation at high-temperature, yielding high water contents in the liebermannite samples (i.e. higher than the amount of water produced by the decomposition of $Al(OH)_3$). We were not able to produce water-free liebermannite samples even with dry pressure materials.

The infrared spectra provide information on water incorporation in liebermannite (**Fig. 6**). Several O-H vibrational modes are observed: (1) the stretching vibrations of weakly hydrogen bound hydroxyl units produce intense bands between 3700 and 3500 $cm^{-1}$; these modes are more pronounced in the 12 GPa sample. (2) The stretching vibrations of both $H_2O$ molecules and more strongly hydrogen bound hydroxyl units occur in the 3425-3100 $cm^{-1}$ wavenumber range; they become dominant in the 15 and 24 GPa samples (**Fig. 6a**). (3) The O-H stretching and bending vibrations of the hydronium ($H_3O^+$) ion are observed near 2900 $cm^{-1}$ and 1665 $cm^{-1}$; these modes disappear at the highest pressure. In the absence of organic contaminants, such as acetone or bond materials, the coexistence of these two modes confirms the presence of $H_3O^+$ in *lowP* liebermannite. (4) The H-O-H bending vibration of the water molecule slightly shifts from 1610 to 1630 $cm^{-1}$ with increasing pressure (**Fig. 6b**). (5) The combination (stretching/bending) modes of both $H_2O$ molecules (near 5200 $cm^{-1}$) and hydroxyl units (near 4500 $cm^{-1}$) display continuous shift to lower frequencies with increasing pressure (**Fig. 6c**). This shift is compatible with the increase of the strength of hydrogen bonds with pressure, as usually observed in minerals (Cynn & Hofmeister, 1994). The observed spectral features suggest the presence of $H_2O$ and $H_3O^+$

283 substituting for $K^+$ in the tunnel (Bethell & Sheppard, 1953) and the substitution of hydrogen ($H^+$)
284 in octahedral sites where it forms O-H bonds with one of the six possible oxygen ions in the vacant
285 octahedral site.

286 The powder X-ray diffraction analyses were conducted on the samples synthesized at 15
287 GPa and 24 GPa. Both patterns can be refined with parameters consistent with the I4/m phase:
288 a = 9.3304(4)Å, c = 2.7223(2)Å. Obtaining the same lattice parameters for the samples out of the
289 different pressures of annealing experiments implies that the liebermannite phase is elastic enough
290 to regain its low-pressure parameters consistent with previous studies (Nishiyama et al., 2005;
291 Sueda et al., 2004).

292

293 **4. Discussion and conclusions**

294 **4. 1 Electrical conduction in liebermannite**

295 The electrical conductivity of K-feldspar before transforming into libermannite exhibit
296 higher electrical conductivity compared to the previous electrical conductivity measurements of
297 F-feldspar reported at 1 GPa (Hu et al., 2013). The high electrical conductivity of K-feldspar
298 observed in our study can be explained by the 0.02 wt. % $H_2O$ contents in our samples, compared
299 to the dry verity reported by Hu et al. 2013 study. Similar electrical behavior has been observed in
300 dry albite and water-bearing albite (Hu et al., 2013; Ni et al., 2011).

301 The electrical conductivity of hydrous liebermannite increases discontinuously upon
302 increasing temperature (**Fig. 2b**). At temperatures below 700 K, conductivity is likely to be
303 dominated by molecular water that is loosely bound in the tunnel sites and the associated activation
304 energy is less than 0.40 eV. In the temperature range between 700 K and 1100 K, the conductivity
305 is likely largely due to extrinsic proton defects that are formed due to coupled substitutions of the

octahedral sites. The associated activation energy varies between 0.64 eV and 0.78 eV. At temperatures above 1200 K, the conductivity is likely to be dominated by fast motions of $K^+$ or $H^+$ ions (from $H_3O^+$) ions in the channel. The associated activation energy is greater than 0.82 eV. Higher conductivity has also been observed in alkali bearing materials with the hollandite crystal structure (Khanna et al., 1981). Such higher conductivity is often referred to as super-ionic conductivity (He et al., 2016; Khanna et al., 1981). In our study, we are documenting such effects at extreme pressures of 12 to 24 GPa in libermannite.

The electrical conductivity of minor phases, wadeite, stishovite, and kyanite should not interfere with the measured conductivity of liebermannite due to their low volume fractions (occur as isolated grains). Based on chemical analyses of individual liebermannite grains in our samples, we observe a maximum of 7 % $K^+$ site vacancy in our liebermannite after electrical conductivity measurements at 12, 15, and 24 GPa. The intrinsic defects seem to dominate the conduction mechanism at high temperatures, whereas extrinsic defects may be responsible for the observed conductivity at lower temperatures.

### 4.2 Water incorporation in liebermannite

The occurrence of several OH stretching bands (Fig. 4a) suggests that different substitution mechanisms take place, including $H^+$ substitution in octahedral sites and $H_2O/H_3O^+$ in tunnels, resulting in distinct hydrogen bonding strengths. Protons attachment to both bridging and non-bridging oxygen can also help to explain such a wide range of OH stretching vibrations. Strong pleochroism in the 3500-3600 $cm^{-1}$ range of the polycrystalline sample at 12 GPa indicates the random orientation of the crystals, in contrast to higher pressure samples. Water/hydrogen could be incorporated in liebermannite structure in a variety of sites including the substitution of $H^+$ in

the silicon octahedral sites, i.e., $Si_{Si}^{4+} = Al_{Si}^{3+} + H_{Si}^{1+}$ or $Si_{Si}^{4+} = 4H_{Si}^{1+}$, the substitution of $H^+$ in the aluminum octahedral site $Al_{Al}^{3+} = 3H_{Al}^{1+}$, the substitution of $H^+$ and $H_3O^+$ in the potassium site ($K_K^{1+} = H_K^{1+}$, or $K_K^{1+} = (H_3O)_K^{1+}$) and accommodation of molecular $H_2O$ in the tunnel as in $KAlSi_3O_8 + H_2O = KAlSi_3O_8 \cdot H_2O$. The chemical analyses provide crucial information on possible coupled substitution mechanisms for hydrogen incorporation in liebermannite. The slight deficiency in silicon and increase in aluminum observed in some liebermannite grains ($K_{0.957\pm0.044}Al_{1.090\pm0.057}Si_{2.931\pm0.032}O_8$) is consistent with a reaction involving a substitution in the distorted octahedral with the direct replacement of $Si^{4+}$ by $Al^{3+}$ and $H^+$ or by $4H^+$. The chemical analyses also indicate a slight aluminum deficiency in some crystals ($K_{1.00}Al_{0.983}Si_{3.01}O_8$). This may suggest possible proton substitution in the octahedral site, replacing $Al^{3+}$ with $3H^+$.

As the *hiP* liebermannite is considered the dominant polymorph throughout the Earth's lower mantle, knowledge on water solubility in the *hiP* structure becomes crucial to assess the transport of $H_2O$ to the deepest lower mantle regions through deep extending slabs. Given the positive clapeyron slope of P (GPa) = 16.6 + 0.007 K (T) between the *lowP* and *hiP* liebermannite and assuming that trace quantity of water is unlikely to affect the slope, the hydrous liebermannite sample synthesized at 24 GPa and 1500 K is expected to be the *lowP* polymorph with tetragonal symmetry (Nishiyama et al., 2005). However, upon a decrease of temperature to 1000 K, at constant pressure, the sample is likely to transform to *hiP* liebermannite with monoclinic symmetry (Nishiyama et al., 2005). Upon structural transformation from *lowP* to *hiP* liebermannite, the electrical resistivity measurements of the sample do not indicate a discontinuous decrease of the electrical resistance, which indicates the release of free fluid phase or hydrous melting in the sample (Freitas & Manthilake, 2019). Assuming that the water incorporation into the liebermannite structure occurs at the highest temperature, this crucial observation suggests that the *hiP*

liebermannite structure is capable of sequestering $H^+$ into octahedral sites as molecular $H_2O$ or ionic $H_3O^+$ in its structure similar to the *lowP* liebermannite. The incorporation of $H_2O$ has been observed in both naturally occurring tetragonal and monoclinic hollandite crystal structures with different stoichiometry (Miura, 1986), thus confirming our observations on liebermannite. The micro Raman grid-analyses of our samples after electrical conductivity measurements indicate the absence of melt phases, confirming that the water expulsion may not occur in our samples at high temperatures.

Due to the small grain sizes (< 5 μm), infrared analyses in these minor phases were not possible; nevertheless, absence of peaks in the high-wavenumber region of the Raman spectra of wadeite and Al-free stishovite indicates that water is not present within their crystal structure (**Fig. 7**). However, $H_2O$ contents up to 3 wt. % have been observed in stishovite containing aluminum (Litasov et al., 2007; Yoshino et al., 2014). IR spectral features of Al-free stishovite exhibit some similarities with those of liebermannite in the spectral range from 3111 to 3261 (Litasov et al., 2007). Particularly peak position of 3117 $cm^{-1}$ in the sample synthesized at 15 GPa (**Fig. 7a**) overlaps the main peak position of stishovite at 3117 $cm^{-1}$ observed for Al- free and Al-bearing stishovite (Yoshino et al., 2014). In order to confirm that the spectral feature at 3117 $cm^{-1}$ in libermannite, we have analyzed the O-H region of the Raman spectra of stishovite in the 15 GPa sample. The observed water-free conditions (**Fig 7a**) strongly suggests the spectral feature at 3117 $cm^{-1}$ observed in libermannite could be unrelated to stishovite, rather a spectral feature characteristic of libermannite. We conclude that the similarities btween libermannite and stishovite may be related to similar substitution mechanisms of hydrogen in octahedral sites $SiO_6$ or $AlO_6$. The preferential partitioning of water into the liebermannite phase over stishovite observed in our samples may be partly due to the low Al content in stishovite that is in equilibrium with

liebermannite (**Table 2**). Therefore, the presence of Al-free stishovite in the studied samples should not influence the IR spectra of liebermannite. Even in the case of very low water contents of about 16-30 wt. ppm observed in Al-free stishovite (Litasov et al., 2007), these should not affect water quantification of liebermannite in this study.

### 4.3 Geophysical implications

The upper mantle underneath the Philippine Sea (Tarits & Mandéa, 2010) and Northeastern China (Kelbert et al., 2009) is characterized by unusual electrical and seismic wave velocity structures, in particular, electrical conductivities as high as 1 S/m and high-velocity anomalies of up to $+\delta V_P$ 1.5 % and $\delta V_S$ 2.0 % have been observed in these regions. The observed anomalies cannot be readily explained by normal mantle consisting of major mantle phases such as olivine and wadsleyite (Manthilake et al., 2009). If the observed positive velocity anomalies were assumed to be caused by temperature variations alone, the temperature in the uppermost region of the mantle transition zone estimated to be about 800 K below the normal mantle geotherm (Manthilake et al., 2009). The corresponding electrical conductivity of hydrous olivine and wadsleyite for such low temperatures would be significantly lower; as a consequence, the proton conduction in olivine and wadsleyite cannot be responsible for the electrical conductivity observed at the upper mantle and in the mantle transition zone (Manthilake et al., 2009). Similarly, the presence of melt cannot explain the observed anomalies, because even a minor fraction of melt would significantly decrease both the primary ($V_P$) and secondary ($V_S$) wave velocities (Chantel et al., 2016; Freitas et al., 2017; Weidner et al., 2018).

Due to superionic conduction properties and high modal abundance (> 30 vol. %) of liebermannite in deeply subducted crustal components, the electrical conduction in slabs is likely

to dominate by the liebermannite. This would make such slab components highly conductive compared to slabs consisting of mafic and ultramafic lithologies (Huang et al., 2005; Yoshino et al., 2008, 2008, 2014). However, the presence of liebermannite alone cannot account for the positive velocity anomaly observed in the upper mantle beneath the Philippine Sea (Tarits & Mandéa, 2010) and northeastern China (Kelbert et al., 2009) because the elastic wave velocities measured in liebermannite are comparable with those of common mantle mineral phases (Caracas & Boffa Ballaran, 2010; Mookherjee & Steinle-Neumann, 2009). Instead, the seismic wave velocities of Al-poor stishovite, another principal mineral phase stable in subducting continental sediments, are notably faster than those of mantle mineral phases (Gréaux et al., 2016). The stishovite co-existing with liebermannite in our samples is noticeably devoid of aluminum (**Table 2**). Here we propose that Al-poor stishovite coexisting with liebermannite in the subducted continental sediments may be responsible for the positive velocity anomaly observed at the mantle transition zone beneath the Philippine Sea (Tarits & Mandéa, 2010) and northeastern China (Kelbert et al., 2009).

Continental crustal portion of the subducted slab, consisting of libermannite, majoritic garnet, and stishovite, are expected to have a higher 0.2 g $cm^{-3}$density than the ambient mantle, but this density relation is overturned at the 660 km discontinuity (Irifune et al., 1994; Nishiyama et al., 2005). This implies that subducting crustal components of the slabs may penetrate into the mantle transition zone, but are prevented from entering the lower mantle (Nishiyama et al., 2005), such as those observed in the Northeastern China subduction system (Ichiki et al., 2006). However, the lower mantle origin of some of the plumes (French & Romanowicz, 2015; Hart et al., 1992) carrying the EM-type components in OIB magmas (Hart et al., 1992) provides strong evidence supporting the presence of recycled continental materials in the lower mantle. We propose that

421 mixing of continental with oceanic sediments may increase the density of sedimentary components
422 facilitating the sinking of slabs towards the core-mantle boundary. The high electrical conductivity
423 observed at a 1200 km depths in the Earth's lower mantle beneath the Philippine sea subduction
424 system (Kelbert et al., 2009; Tarits & Mandéa, 2010) may be linked to such continuous subduction
425 of continental sediments across the mantle transition zone into the Earth's lower mantle (**Fig. 7**).
426 Owing to hotter temperatures relative to the ambient mantle, the rising plume is unlikely
427 to exchange incompatible elements, including water, with the surrounding mantle, including the
428 hydrated MTZ and the upper mantle (Bercovici & Karato, 2003). Thus, it is likely that the $H_2O$
429 present in plume-derived rocks is primarily linked to the deep lower mantle source. The relatively
430 high $H_2O$ contents of OIB derived from deep mantle plumes hint towards the presence of hydrated
431 crustal components present in the deeper part of the lower mantle (**Fig. 8**). While major mineral
432 phases in pyrolitic compositions are almost devoid of $H_2O$ under lower mantle conditions, our
433 study demonstrates that liebermannite could be an important host of $H_2O$ in the Earth's lower
434 mantle. In this scenario, $H_2O$ in the EMII-source OIB is primarily related to deeply subducted
435 continental materials, in which liebermannite is the principal $H_2O$ carrier. On the other hand, the
436 subducted continental materials that may reach the core-mantle boundary would hydrate the HIMU
437 type plume sources together with a possible contribution from *dense hydrous magnesium silicates*
438 (DHMS) (Nishi et al., 2014; Pamato et al., 2014) and primordial $H_2O$ (Dixon et al., 2002).
439
440
441
442
443

**Acknowledgments**

We thank Nathalie Bolfan-Casanova and Maud Boyet for constructive discussion, J-L. Devidal for his assistance with electron microprobe analyses and Emmy Voyer for her assistance with SEM analyses. The constructive and in-depth reviews by the associate Editor, and two reviewers: Lidong Dai and Hongzhan Fei substantially improved the quality of the manuscript. G.M. acknowledges funding from the(INSU-CNRS. M.M. is supported by the US National Science Foundation grants, EAR 1753125, 1763215. This research was financed by the French Government Laboratory of Excellence initiative n°ANR-10-LABX-0006, the Région Auvergne, and the European Regional Development Fund (ClerVolc contribution number xx). The authors comply with AGU's data policy, and the data of this study are available in Figshare.
(https://figshare.com/articles/Water_content_calculations/12179067)
and (https://figshare.com/articles/Experimental_data_xlsx/12179046).
The authors declare no competing financial interests.

**References**

Bercovici, D., & Karato, S.-I. (2003). Whole-mantle convection and the transition-zone water filter. *Nature*, *425*(6953), 39–44. https://doi.org/10.1038/nature01918

Bethell, D. E., & Sheppard, N. (1953). The Infrared Spectrum of the H3O + Ion in Acid Hydrates. *Journal of Chemical Physics*, *21*, 1421. https://doi.org/10.1063/1.1699260

Bolfan-Casanova, N., Keppler, H., & Rubie, D. C. (2003). Water partitioning at 660 km depth and evidence for very low water solubility in magnesium silicate perovskite. *Geophysical Research Letters*, *30*(17), 1905. https://doi.org/10.1029/2003GL017182

Cabral, R. A., Jackson, M. G., Koga, K. T., Rose-koga, E. F., Hauri, E. H., Whitehouse, M. J., et

al. (2014). Volatile cycling of H2O, CO2, F, and Cl in the HIMU mantle: A new window provided by melt inclusions from oceanic hot spot lavas at Mangaia, Cook Islands. *Geochemistry Geophysics Geosystems*, *15*, 4445–4467. https://doi.org/10.1002/2014GC005473.Received

Caracas, R., & Boffa Ballaran, T. (2010). Elasticity of (K,Na)AlSi3O8 hollandite from lattice dynamics calculations. *Physics of the Earth and Planetary Interiors*, *181*(1–2), 21–26. Retrieved from http://dx.doi.org/10.1016/j.pepi.2010.04.004

Chantel, J., Manthilake, G., Andrault, D., Novella, D., Yu, T., & Wang, Y. (2016). Experimental evidence supports mantle partial melting in the asthenosphere. *Science Advances*, *2*(5), e1600246.

Cynn, H., & Hofmeister, A. M. (1994). High-pressure IR spectra of lattice modes and OH vibrations in Fe- bearing wadsleyite. *Journal of Geophysical Research*, *99*(B9), 17717–17727. https://doi.org/10.1029/94jb01661

Deschamps, F., Kaminski, E., & Tackley, P. J. (2011). A deep mantle origin for the primitive signature of ocean island basalt. *Nature Geoscience*, *4*(11), 1–4. https://doi.org/10.1038/ngeo1295

Dixon, J. E., Leist, L., Langmuir, C., & Schilling, J. (2002). Recycled dehydrated lithosphere observed in plume-influenced mid-ocean-ridge basalt. *Nature*, *420*, 385–389.

Fei, H., Druzhbin, D., & Katsura, T. (2020). The Effect of Water on Ionic Conductivity in Olivine. *Journal of Geophysical Research: Solid Earth*, *125*(3). https://doi.org/10.1029/2019JB019313

Ferroir, T., Onozawa, T., Yagi, T., Merkel, S., Miyajima, N., Nishiyama, N., et al. (2006). Equation of state and phase transition in KAlSi3O8 hollandite at high pressure. *American*

*Mineralogist*, *91*, 327–332. https://doi.org/10.2138/am.2006.1879

Freitas, D., & Manthilake, G. (2019). Electrical conductivity of hydrous silicate melts : Implications for the bottom-up hydration of Earth ' s upper mantle. *Earth and Planetary Science Letters*, *523*, 115712. https://doi.org/10.1016/j.epsl.2019.115712

Freitas, D., Manthilake, G., Schiavi, F., Chantel, J., Bolfan-Casanova, N., Bouhifd, M. A., & Andrault, D. (2017). Experimental evidence supporting a global melt layer at the base of the Earth's upper mantle. *Nature Communications*, *8*(1), 2186. https://doi.org/10.1038/s41467-017-02275-9

French, S. W., & Romanowicz, B. (2015). Broad plumes rooted at the base of the Earth's mantle beneath major hotspots. *Nature*, *525*(7567), 95–99. https://doi.org/10.1038/nature14876

Fu, S., Yang, J., Karato, S. ichiro, Vasiliev, A., Presniakov, M. Y., Gavrilliuk, A. G., et al. (2019). Water Concentration in Single-Crystal (Al,Fe)-Bearing Bridgmanite Grown From the Hydrous Melt: Implications for Dehydration Melting at the Topmost Lower Mantle. *Geophysical Research Letters*, *46*(17–18), 10346–10357. https://doi.org/10.1029/2019GL084630

Furusawa, S., Suemoto, T., & Ishigame, M. (1988). Quasielastic light scattering in the one-dimensional superionic conductor hollandites. *Physical Review B*, *38*(17), 12600–12606.

Gréaux, S., Kono, Y., Wang, Y., Yamada, A., Zhou, C., Jing, Z., et al. (2016). Sound velocities of aluminum-bearing stishovite in the mantle transition zone. *Geophysical Research Letters*, *43*, 4239–4246. https://doi.org/10.1002/2016GL068377.Received

Hacker, B. R. (2008). H2O subduction beyond arcs. *Geochemistry Geophysics Geosystems*, *9*(3), Q03001. https://doi.org/10.1029/2007GC001707

Hart, S. R. (1988). Heterogeneous mantle domains : signatures , genesis and mixing

chronologies. *Earth and Planetary Science Letters*, *90*, 273–296.

Hart, S. R., Hauri, E. H., Oschmann, L. A., & Whitehead, J. A. (1992). Mantle Plumes and Entrainment : Isotopic Evidence. *Science*, *256*, 517–521.

He, Y., Sun, Y., Lu, X., Gao, J., Li, H., & Li, H. (2016). First-principles prediction of fast migration channels of potassium ions in KAlSi3O8 hollandite: Implications for high conductivity anomalies in subduction zones. *Geophysical Research Letters*, *43*(12), 6228–6233. https://doi.org/10.1002/2016GL069084.Received

van der Hilst, R. D., Widiyantoro, S., & Engdahl, E. R. (1997). Evidence for deep mantle circulation from global tomography. *Nature*, *386*, 578–584. Retrieved from http://dx.doi.org/10.1038/386578a0

Hirschmann, M. M. (2006). Water, Melting, and the Deep Earth H2O Cycle. *Annual Review of Earth and Planetary Sciences*, *34*(1), 629–653. https://doi.org/10.1146/annurev.earth.34.031405.125211

Hu, H., Li, H., Dai, L., Shan, S., & Zhu, C. (2013). Electrical conductivity of alkali feldspar solid solutions at high temperatures and high pressures. *Physics and Chemistry of Minerals*, *40*(1), 51–62. https://doi.org/10.1007/s00269-012-0546-4

Huang, X., Xu, Y., & Karato, S. (2005). Water content in the transition zone from electrical conductivity of wadsleyite and ringwoodite. *Nature*, *434*(7034), 746–749. https://doi.org/10.1038/nature03426

Ichiki, M., Baba, K., Obayashi, M., & Utada, H. (2006). Water content and geotherm in the upper mantle above the stagnant slab : Interpretation of electrical conductivity and seismic P-wave velocity models. *Physics of the Earth and Planetary Interiors*, *155*, 1–15. https://doi.org/10.1016/j.pepi.2005.09.010

Irifune, T., Ringwood, A. E., & Hibberson, W. O. (1994). Subduction of continental crust and terrigenous and pelagic sediments: an experimental study. *Earth and Planetary Science Letters*, *126*, 351–368.

Katsura, T., Sato, K., & Ito, E. (1998). Electrical conductivity of silicate perovskite at lower-mantle conditions. *Nature*, *395*(October), 493–495. https://doi.org/10.1038/26736

Katsura, T., Yoneda, A., Yamazaki, D., Yoshino, T., Ito, E., Suetsugu, D., et al. (2010). Adiabatic temperature profile in the mantle. *Physics of the Earth and Planetary Interiors*, *183*(1–2), 212–218. https://doi.org/10.1016/j.pepi.2010.07.001

Kawai, K., & Tsuchiya, T. (2013). First-principles study on the high-pressure phase transition and elasticity of KAlSi3O8 hollandite. *American Mineralogist*, *98*, 207–218. https://doi.org/10.2138/am.2007.2246

Kelbert, A., Schultz, A., & Egbert, G. (2009). Global electromagnetic induction constraints on transition-zone water content variations. *Nature*, *460*(7258), 1003–1006. https://doi.org/10.1038/nature08257

Khanna, S. K., Gruner, G., Orbach, R., & Beyeler, H. U. (1981). Thermally Activated Microwave Conductivity in the Superionic Conductor Hollandite (K1.54Mg0.77Ti7.23O16). *Physical Review Letters*, *47*(4), 255–257.

Koch-Müller, M., & Rhede, D. (2010). IR absorption coefficients for water in nominally anhydrous high-pressure minerals. *American Mineralogist*, *95*(5–6), 770–775. https://doi.org/10.2138/am.2010.3358

Litasov, K. D., Kagi, H., Shatskiy, A., Ohtani, E., Lakshtanov, D. L., Bass, J. D., & Ito, E. (2007). High hydrogen solubility in Al-rich stishovite and water transport in the lower mantle. *Earth and Planetary Science Letters*, *262*, 620–634.

https://doi.org/10.1016/j.epsl.2007.08.015

Manthilake, G., Matsuzaki, T., Yoshino, T., Yamashita, S., Ito, E., & Katsura, T. (2009). Electrical conductivity of wadsleyite as a function of temperature and water content. *Physics of the Earth and Planetary Interiors*, *174*(1–4), 10–18. https://doi.org/10.1016/j.pepi.2008.06.001

Manthilake, G., Mookherjee, M., Bolfan-Casanova, N., & Andrault, D. (2015). Electrical conductivity of lawsonite and dehydrating fluids at high pressures and temperatures. *Geophysical Research Letters*, *42*(18), 7398–7405. https://doi.org/10.1002/2015GL064804

Miura, H. (1986). The crystal structure of hollandite. *Mineralogical Journal*, *13*(3), 119–129.

Mookherjee, M., & Steinle-Neumann, G. (2009). Detecting deeply subducted crust from the elasticity of hollandite. *Earth and Planetary Science Letters*, *288*(3–4), 349–358. https://doi.org/10.1016/j.epsl.2009.09.037

Ni, H., Keppler, H., Manthilake, M. A. G. M., & Katsura, T. (2011). Electrical conductivity of dry and hydrous NaAlSi3O8 glasses and liquids at high pressures. *Contributions to Mineralogy and Petrology*, *162*(3), 501–513. https://doi.org/10.1007/s00410-011-0608-5

Nishi, M., Irifune, T., Tsuchiya, J., Tange, Y., Nishihara, Y., Fujino, K., & Higo, Y. (2014). Stability of hydrous silicate at high pressures and water transport to the deep lower mantle. *Nature Geoscience*, *7*, 224–227. https://doi.org/10.1038/NGEO2074

Nishiyama, N., Rapp, R. P., Irifune, T., Sanehira, T., Yamazaki, D., & Funakoshi, K. I. (2005). Stability and P – V – T equation of state of KAlSi3O8 -hollandite determined by in situ X-ray observations and implications for dynamics of subducted continental crust material. *Physics and Chemistry of Minerals*, *32*, 627–637. https://doi.org/10.1007/s00269-005-0037-y

582 Ohta, K., Hirose, K., Ichiki, M., Shimizu, K., Sata, N., & Ohishi, Y. (2010). Electrical
583 conductivities of pyrolitic mantle and MORB materials up to the lowermost mantle
584 conditions. *Earth and Planetary Science Letters*, *289*(3–4), 497–502.
585 https://doi.org/10.1016/j.epsl.2009.11.042
586 Pamato, M. G., Myhill, R., Boffa Ballaran, T., Frost, D. J., Heidelbach, F., & Miyajima, N.
587 (2014). Lower-mantle water reservoir implied by the extreme stability of a hydrous
588 aluminosilicate. *Nature Geoscience*, *8*, 75–79. https://doi.org/10.1038/NGEO2306
589 Rodriguez-Carvajal, J. (1993). Recent advances in magnetic structure determination by neutron
590 powder diffraction. *Physica B: Condensed Matter*, *192*, 55–69.
591 Schiavi, F., Bolfan-Casanova, N., Withers, A. C., Médard, E., Laumonier, M., Laporte, D., et al.
592 (2018). Water quantification in silicate glasses by Raman spectroscopy: Correcting for the
593 effects of confocality, density and ferric iron. *Chemical Geology*, *483*(March), 312–331.
594 https://doi.org/10.1016/j.chemgeo.2018.02.036
595 Schmidt, M. W. (1996). Experimental Constraints on Recycling of Potassium from Subducted
596 Oceanic Crust. *Science*, *272*(5270), 1927–1930.
597 https://doi.org/10.1126/science.272.5270.1927
598 Sinmyo, R., Pesce, G., Greenberg, E., McCammon, C., & Dubrovinsky, L. (2014). Lower mantle
599 electrical conductivity based on measurements of Al, Fe-bearing perovskite under lower
600 mantle conditions. *Earth and Planetary Science Letters*, *393*, 165–172.
601 https://doi.org/10.1016/j.epsl.2014.02.049
602 Smyth, J. R., & Jacobsen, S. D. (2006). Nominally anhydrous minerals and Earth ' s deep water
603 cycle. (S. van der Lee & S. D. Jacobsen, Eds.), *American Geophysical Union Monograph*
604 *Series*. Washington DC: American Geophysical Union.

605 Sueda, Y., Irifune, T., Nishiyama, N., Rapp, R. P., Ferroir, T., Onozawa, T., et al. (2004). A new
606 high-pressure form of KAlSi3O8 under lower mantle conditions. *Geophysical Research*
607 *Letters*, *31*(23), 1–4. https://doi.org/10.1029/2004GL021156
608 Syracuse, E. M., Keken, P. E. Van, Abers, G. A., van Keken, P. E., Abers, G. A., Suetsugu, D.,
609 et al. (2010). The global range of subduction zone thermal models. *Physics of the Earth and*
610 *Planetary Interiors*, *183*(1–2), 73–90. https://doi.org/10.1016/j.pepi.2010.02.004
611 Tarits, P., & Mandéa, M. (2010). The heterogeneous electrical conductivity structure of the
612 lower mantle. *Physics of the Earth and Planetary Interiors*, *183*, 115–125.
613 https://doi.org/10.1016/j.pepi.2010.08.002
614 Urakawa, S., Kondo, T., Igawa, N., Shimomura, O., & Ohno, H. (1994). Synchrotron Radiation
615 Study on the High-Pressure and High-Temperature Phase Relations of KAISi3O8. *Physics*
616 *and Chemistry of Minerals*, *21*, 387–391.
617 Weidner, D. J., Li, L., Whitaker, M. L., & Triplett, R. (2018). Ultrasonic Acoustic Velocities
618 During Partial Melting of a Mantle Peridotite KLB-1. *Journal of Geophysical Research:*
619 *Solid Earth*, *123*(2), 1252–1261. https://doi.org/10.1002/2017JB014753
620 Willbold, M., & Stracke, A. (2006). Trace element composition of mantle end-members:
621 Implications for recycling of oceanic and upper and lower continental crust. *Geochemistry*
622 *Geophysics Geosystems*, *7*, Q04004. https://doi.org/10.1029/2005GC001005
623 Yoshikado, S., Ohachi, T., Taniguchi, I., Onoda, Y., Watanabe, M., & Fujiki, Y. (1982). Ionic
624 conductivity of hollandite type compounds from 100 Hz to 37.0 GHz. *Solid State Ionics*, *7*,
625 335–344.
626 Yoshino, T., Manthilake, G., Matsuzaki, T., & Katsura, T. (2008). Dry mantle transition zone
627 inferred from the conductivity of wadsleyite and ringwoodite. *Nature*, *451*(7176), 326–329.

https://doi.org/10.1038/nature06427

Yoshino, T., Nishi, M., Matsuzaki, T., Yamazaki, D., & Katsura, T. (2008). Electrical conductivity of majorite garnet and its implications for electrical structure in the mantle transition zone. *Physics of the Earth and Planetary Interiors*, *170*(3–4), 193–200. https://doi.org/10.1016/j.pepi.2008.04.009

Yoshino, T., Shimojuku, A., & Li, D. (2014). Electrical conductivity of stishovite as a function of water content. *Physics of the Earth and Planetary Interiors*, *227*, 48–54. https://doi.org/10.1016/j.pepi.2013.12.003

Yoshino, T., Kamada, S., Zhao, C., Ohtani, E., & Hirao, N. (2016). Electrical conductivity model of Al-bearing bridgmanite with implications for the electrical structure of the Earth's lower mantle. *Earth and Planetary Science Letters*, *434*, 208–219. https://doi.org/10.1016/j.epsl.2015.11.032

## Figures

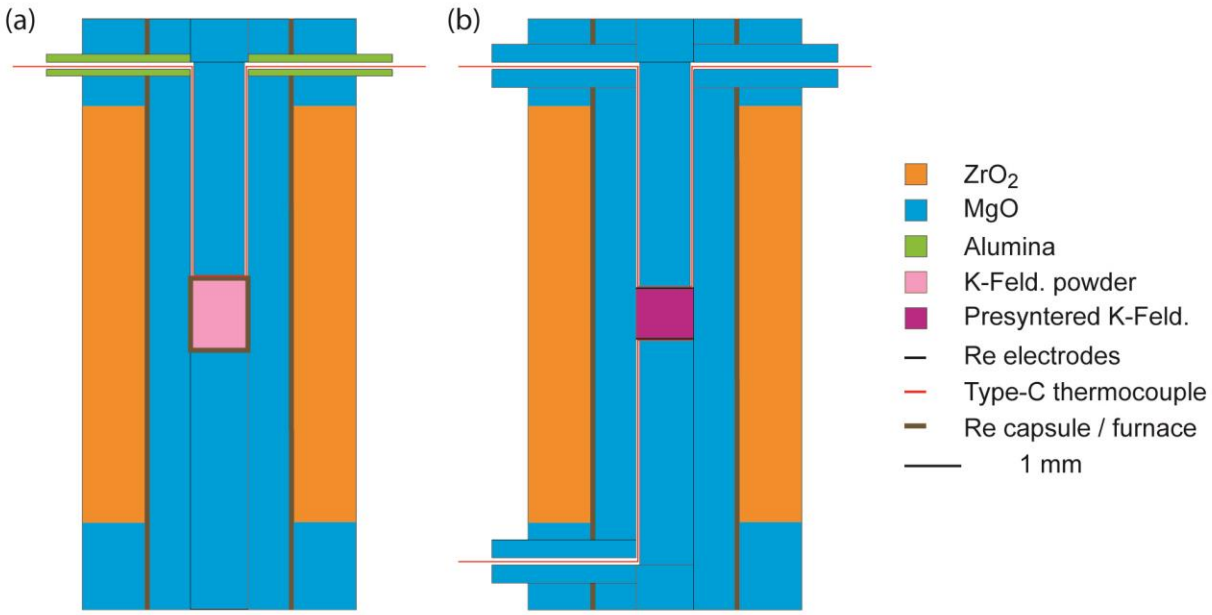


**Fig.1. A schematic cross-section of the assembly. (a) Used for the synthesis of K-feldspar. (b) For electrical conductivity measurements at high-pressure and high-temperature.** The three-electrode configuration for electrical conductivity, which designed to avoid electrode leads sharing the same tungsten carbide anvil in the KAWAI-cell, is expected to improve the insulation resistance of the assembly.

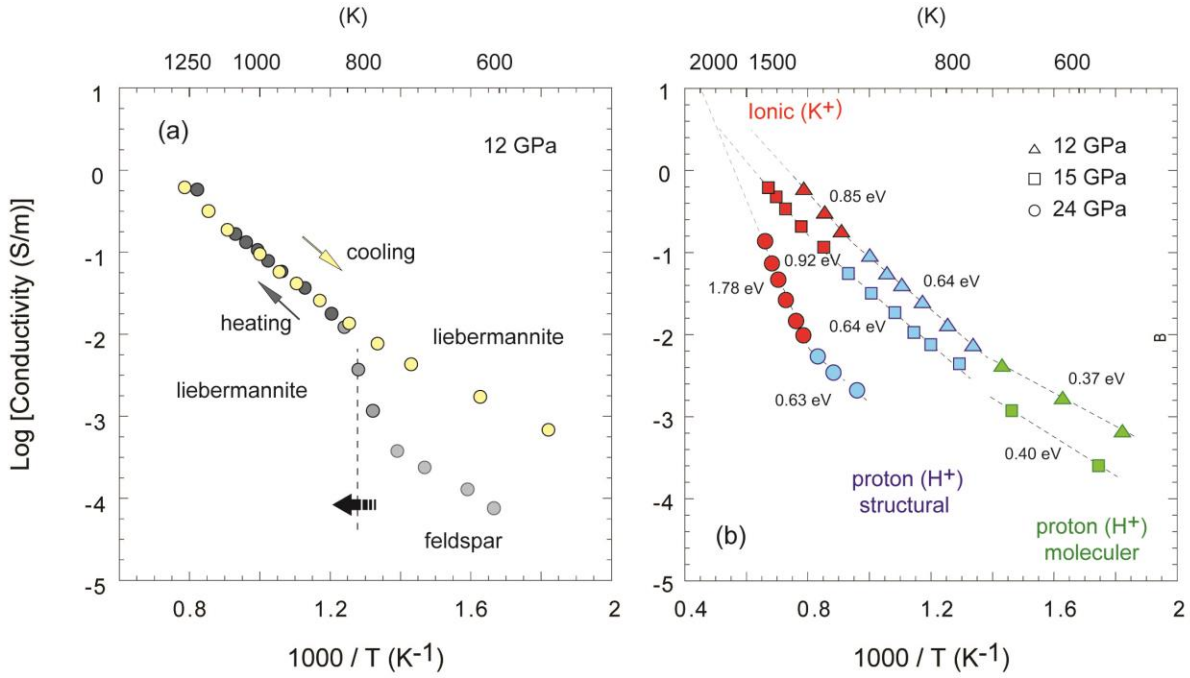


**Fig. 2. The electrical conductivity of liebermannite as a function of inverse temperature. (a)** A plot of the logarithm of electrical conductivity as a function of inverse temperature. The transformation of K-feldspar to liebermannite occurred above 600 K resulting in more than one order of magnitude increase of conductivity. (b) Liebermannite at pressures 12, 15, and 24 GPa. Different conduction mechanisms are labeled in different colors. The activation enthalpies are shown next to individual fitting lines. The error bars associated with the electrical conductivity data measurements are less than the symbol size at high temperatures.

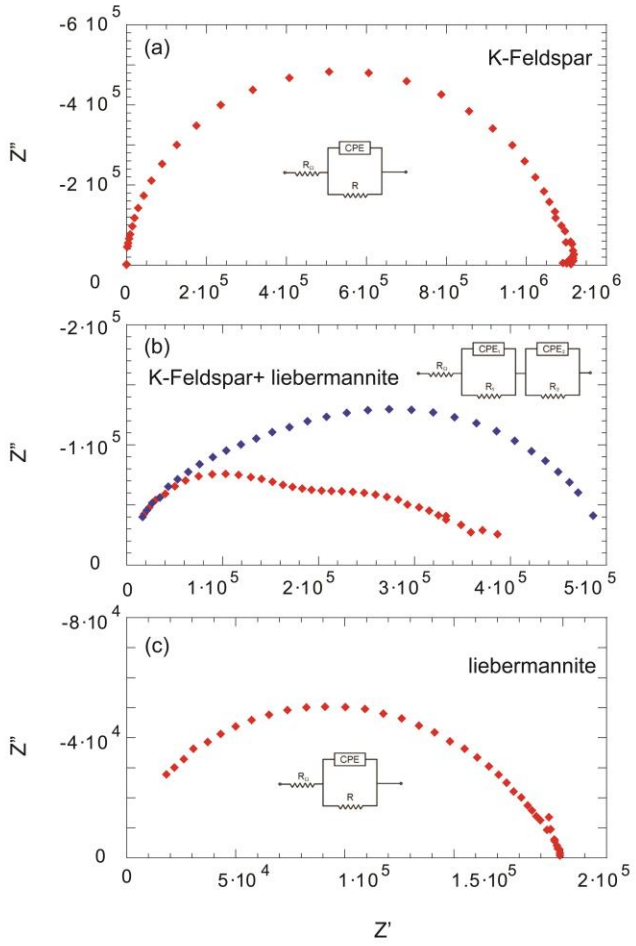


**Fig. 3.** Impedance spectra of the sample at different stages of heating at 12 GPa. (a) at 500 K electrical conductivity of K-feldspar before transforming into liebermannite, (b) at 718 K and 750 K, on the onset of the phase transformation, the second arc in the spectra develops. These additional arcs correspond to the formation of liebermannite. (c) At 850 K, after the complete transformation into liebermannite, there is a significant increase in the sample resistance. The sample resistance is due to the single conductive libermannite phase. The corresponding equivalent circuit.

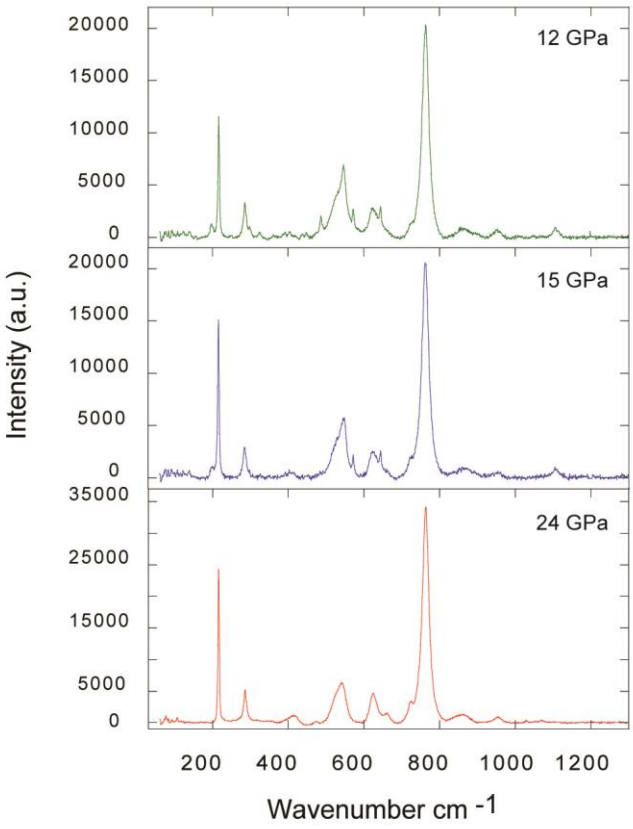


**Fig. 4.** Raman spectra of liebermannite at 12, 15, and 24 GPa.

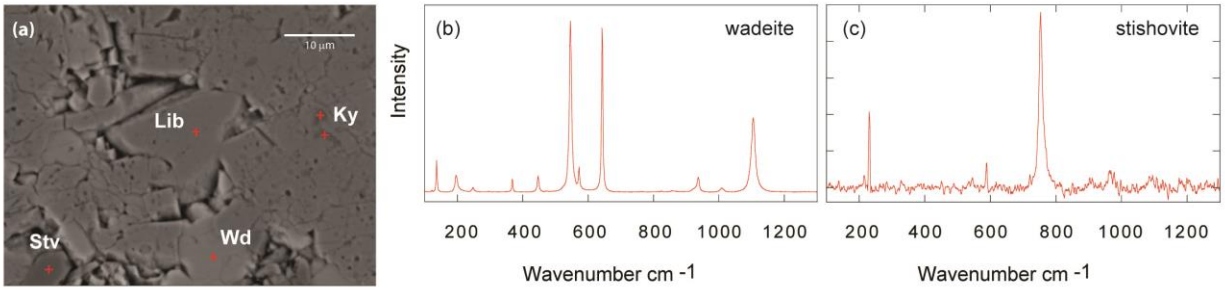


**Fig. 5. Mineral assemblages of the recovered sample.** (a) A back-scattered electron image showing the mineral assemblage at 15 GPa. (b, c) Low-wavenumber bands corresponding to vibrations of the alumino-silicate network; (b) wadeite, (c) stishovite.

742

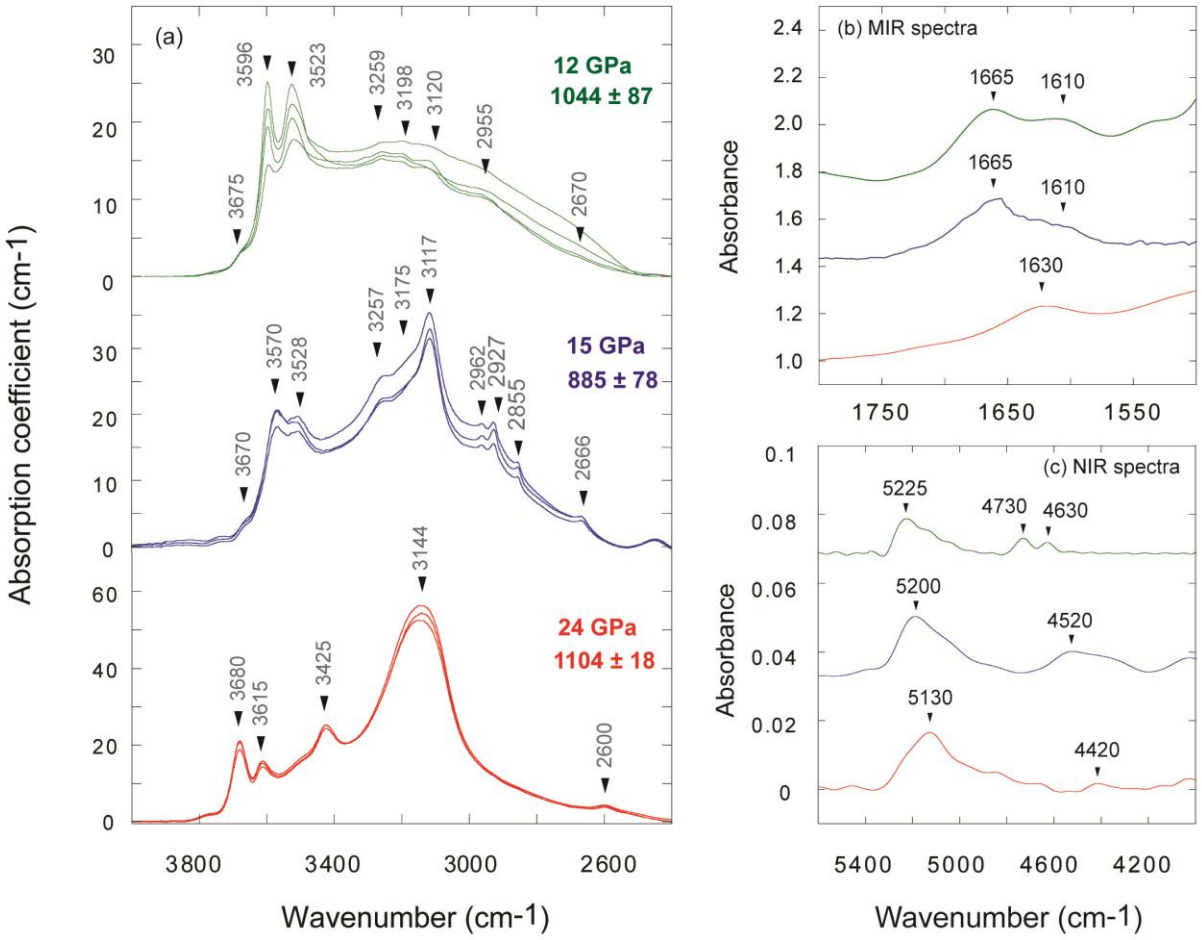


743

744

745

746 **Fig. 6. FTIR spectra of liebermannite. (a)** Near IR spectra of samples synthesized at 12 (green
747 lines), 15 (blue lines), and 24 (red lines) GPa. The calculated $H_2O$ contents (ppm wt.) are indicated
748 next to spectra. **(b)** Middle IR spectra of the three samples showing bending modes of $H_2O$
749 molecules and $H_3O^+$ ions. **(c)** High-wavenumber IR region displaying bands at ~5200 (stretching
750 vibrations of $H_2O$) and 4500-4700 $cm^{-1}$ (O-H stretching vibrations). The peak at 4170 $cm^{-1}$ could
751 be related to H-H vibrations.

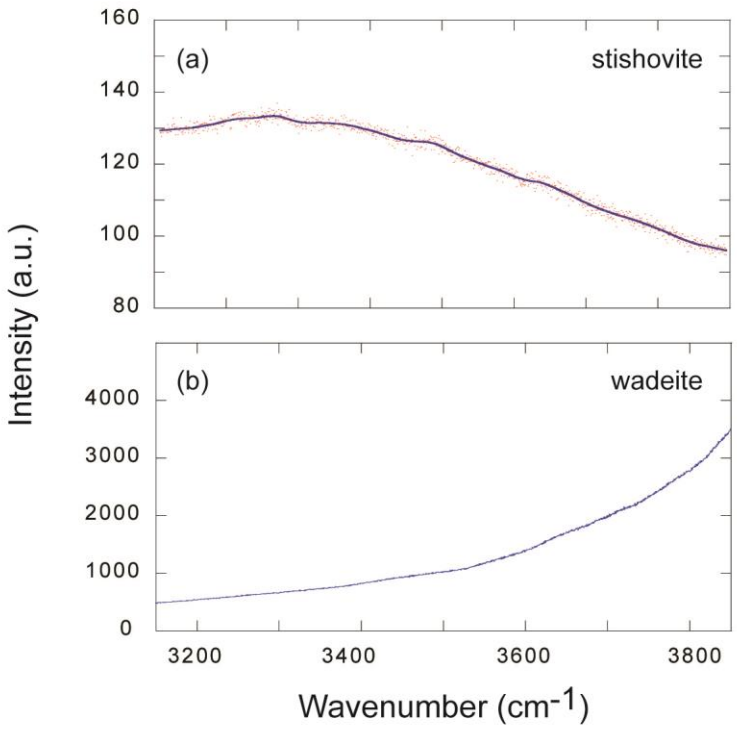


**Fig. 7. Raman spectra of minor phases observed at the sample synthesized at 15 GPa.** The background uncorrected Raman spectra in the O-H region of stishovite (a) and wadeite (b), co-existing with liebermannite. The background noise of the Raman spectrum of stishovite was smoothed using the loess regression method shown in the blue line. Both indicate water absent conditions in their crystal structure. Raman analyses of kyanite were not possible due to their small grain sizes.

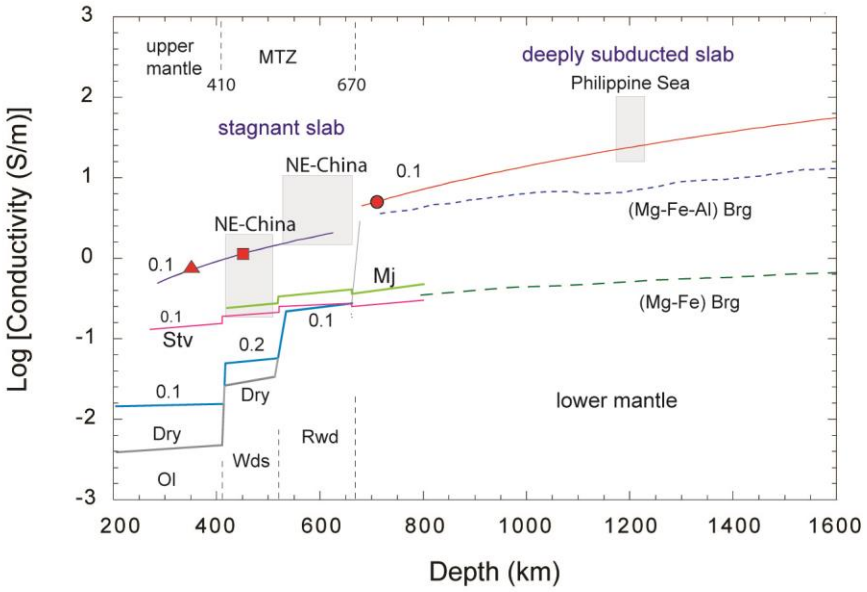


**Fig. 8. Comparison of electrical conductivities of liebermannite with global and regional electrical conductivity profiles.** The blue and red lines correspond to the extrapolation of electrical conductivity along the relevant subduction geotherms (Syracuse et al., 2010), and along the adiabatic geotherm in the lower mantle (Katsura et al., 2010), respectively. The red shaded triangle, square, and the circle indicate the electrical conductivity of liebermannite at 12, 15, and 24 GPa, respectively. The gray shaded boxes indicate the conductivity profiles of NE-China (Kelbert et al., 2009) and the Philippine Sea (Tarits & Mandéa, 2010). The electrical conductivity profiles of dry (black lines) and wet (blue lines) olivine, wadsleyite, ringwoodite (Yoshino et al., 2008), stishovite with 0.1 wt% of $H_2O$ (Yoshino et al., 2014) (pink lines) and majorite garnet (Yoshino et al., 2008) (light green lines) are shown for comparison. The electrical conductivity of (Mg, Fe) bridgmanite (Katsura et al., 1998) (green dashed line) and (Mg, Fe, Al) bridgmanite (Ohta et al., 2010; Sinmyo et al., 2014; Yoshino et al., 2016) (blue dashed line), extrapolated along the adiabatic geotherm in the lower mantle (Katsura et al., 2010), are shown for comparison. The numbers next to conductivity lines are the water contents in wt. %.

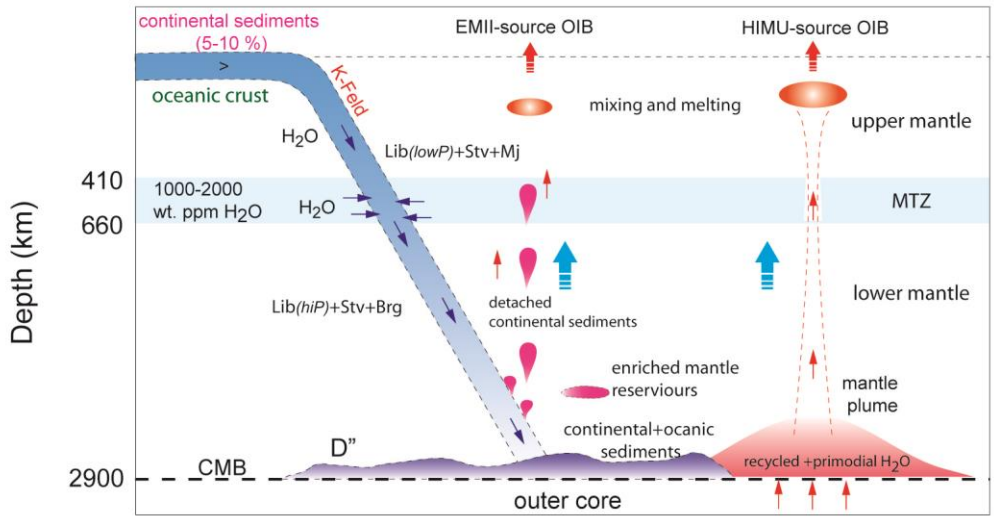


**Fig. 9. The potential mechanism explaining the elevated $H_2O$ content in ocean island basalts.** K-feldspar in subducting continental sediments transforms to liebermannite above 8 GPa and continues to be stable down to the core-mantle boundary conditions. Most of the $H_2O$ carried to the lower mantle by deep penetrating slabs may have been incorporated into the slab at the surface. However, due to the imbalance of the mass of $H_2O$ transported to the Mantle Transition Zone (MTZ) via subduction (Hacker, 2008) and the estimated mass of H2O stored in MTZ based on H2O contents of constituent phases (Freitas & Manthilake, 2019), extraction of H2O from MTZ to the lower mantle can be expected. Because of the ability of libermannite to accommodate several wt. % of the water in its structure (both in lattice defects and the tunnel structures), we argue that libermannite could be a possible carrier of water from the MTZ to the lower mantle. In this two-step, H2O conveyor process, the extraction of H2O by rehydration of deep penetrating slabs at the MTZ would be a likely scenario. Depending on gravitational stability, the subducting continental sediment component may detach from deep-extending slabs, rise through the mantle forming EMII-source OIB, in which liebermannite is the principal water carrier. Some continental sediments may reach the CMB and provide $H_2O$ for HIMU-source lower mantle-derived plumes. (Lib: liebermannite, Sa: K-feldspar, Mj: majorite garnet, Brg: bridgmanite, Stv; stishovite).

826 # List of tables

827

**Table 1.** The reference pre-exponential factor Log$\sigma_0$ and the activation enthalpy in eV for liebermannite at 12, 15, and 24 GPa and their respective water contents.

| Pressure (GPa) | Temperature (K) | Log $\sigma_0$ * (S/m) | Log $\sigma_0$ ** (S/m) | $\Delta H$ * (eV) | $\Delta H$ ** (eV) | $H_2O$ contents ppm wt. |
|---|---|---|---|---|---|---|
| 12 | 550 -750 | 0.57 | n.a | 0.37 | n.a. | 1044 ± 87 |
| | 750 - 1100 | 2.19 | 2.32 | 0.64 | 0.78 | |
| | >1100 | 3.14 | 3.88 | 0.85 | 0.82 | |
| 15 | 573 - 683 | 0.58 | n.a | 0.4 | n.a. | 885 ± 78 |
| | 773 -1173 | 1.76 | 1.61 | 0.64 | 0.76 | |
| | > 1173 | 2.78 | 3.96 | 0.92 | 0.83 | |
| 24 | 1040 - 1200 | 0.38 | 0.24 | 0.63 | 0.76 | 1104 ± 18 |
| | > 1270 | 5 | 8.26 | 1.78 | 0.89 | |

* parameters from individual fitting

** parameters from single fit

n.a: not nalyzed

828

829 **Table 2.** Chemical composition of the constituent mineral phases.

830
831
832
833
834
835
836
837
838
839
840
841
842
843
844
845
846
847
848

849

**Table 2.** Chemical composition of the constituent mineral phases.

| | **Liebermannite** | | | **Wadeite** | | **Stishovite** | | **Kyanite** | |
|---|---|---|---|---|---|---|---|---|---|
| | **12 GPa** | **15 GPa** | **24 GPa** | **12 GPa** | **15 GPa** | **12 GPa** | **15 GPa** | **12 GPa** | **15 GPa** |
| **$SiO_2$** | 64.44 (0.7) | 63.91 (2.5) | 66.70 (0.2) | 73.00 (0.9) | 71.82 (0.5) | 100.50 (0.8) | 101.13 (0.5) | 38.23 (0.9) | 39.11 (0.9) |
| **$K_2O$** | 16.47 (0.4) | 16.18 (1.2) | 16.42 (1.8) | 27.16 (0.8) | 28.22 (0.6) | 0.06 (0.3) | 0.13 (0.07) | 0.15 (0.06) | 0.61 (0.4) |
| **$Al_2O_3$** | 18.98 (0.3) | 20.4 (2.9) | 17.21 (2.0) | 0.15 (0.1) | 0.6 (0.5) | 0.05 (0.2) | 0.07 (0.03) | 62.6 (1.2) | 61.35 (1.2) |
| **Total** | **99.89** | **100.49** | **100.33** | **100.31** | **100.64** | **100.62** | **101.33** | **100.98** | **101.07** |

The standard deviation indicated in parenthesis.

850